Simulations of aerosol-cloud-dynamical feedbacks resulting from entrainment of aerosol into the marine boundary layer during the Atlantic Stratocumulus Transition Experiment

Hongli Jiang
Department of Atmospheric Science, Colorado State University, Fort Collins, Colorado, USA

Graham Feingold
Environmental Technology Laboratory, NOAA, Boulder, Colorado, USA

William R. Cotton
Department of Atmospheric Science, Colorado State University, Fort Collins, Colorado, USA

Received 14 November 2001; revised 21 March 2002; accepted 17 April 2002; published 31 December 2002.

[1] Numerical simulations of a cloudy marine boundary layer (MBL) observed during the Atlantic Stratocumulus Transition Experiment were performed to study the influence of entrainment of free tropospheric cloud condensation nuclei (CCN) on cloud microphysics, dynamics, and radiative properties. The initial CCN concentration is 100 cm^{-3} in one simulation, while in the second simulation it varies from 100 cm^{-3} below the cloud top to a peak of 1200 cm^{-3} at the inversion. In the clean case, cooling from evaporating drizzle destabilizes the layer just below cloud base (not the entire subcloud layer) with respect to the surface, and promotes stronger penetrating cumulus. In the case with the elevated pollution layer, reduced drizzle at the cloud base results in weaker penetrating cumulus and a less effective supply of surface moisture to the cloud. This results in a much lower liquid water path (LWP) relative to the clean case that offsets the cloud albedo enhancement due to higher drop concentrations. Thus, although entrained CCN enhance the droplet concentration, the net effect on the cloud albedo is small. Additional simulations were performed to study the sensitivity of the MBL to varying levels of large-scale subsidence. The change in large-scale subsidence has a large effect on boundary layer dynamics, cloud microphysics, and the radiative budget. The simulations are used to separate the effects of enhanced albedo due to enhanced drop concentrations at constant LWP and those where LWP is modified due to dynamical feedbacks. For this case study, weaker subsidence results in a cloud with higher LWP and a cloud albedo that is enhanced over and above that due to enhanced droplet concentration. The simulations point to the complex dynamical-microphysical-radiative feedbacks in the MBL and how elevated polluted layers can change cloud radiative forcing in ways that would not be easily predicted by large-scale models. *INDEX TERMS:* 0305 Atmospheric Composition and Structure: Aerosols and particles (0345, 4801); 0320 Atmospheric Composition and Structure: Cloud physics and chemistry; 3307 Meteorology and Atmospheric Dynamics: Boundary layer processes; 3337 Meteorology and Atmospheric Dynamics: Numerical modeling and data assimilation; *KEYWORDS:* aerosol-cloud-dynamic feedbacks, entrainment, ASTEX, marine boundary layer, LES

Citation: Jiang, H., G. Feingold, and W. R. Cotton, Simulations of aerosol-cloud-dynamical feedbacks resulting from entrainment of aerosol into the marine boundary layer during the Atlantic Stratocumulus Transition Experiment, *J. Geophys. Res.*, *107*(D24), 4813, doi:10.1029/2001JD001502, 2002.

1. Introduction

[2] Free tropospheric polluted continental air frequently flows over the clean subtropical marine boundary layer [*Albrecht et al.*, 1995] and the Arctic boundary layer [*Curry et al.*, 2000]. This results in polluted air penetrating from the free troposphere downward into the boundary layer and has the potential to alter boundary layer clouds, their radiative properties, and dynamics.

[3] From the perspective of aerosol-cloud-climate feedbacks, the entrainment of polluted air into relatively clean boundary layers is particularly interesting. The traditional concept of enhanced aerosol concentrations resulting in enhanced drop concentrations, and more reflective clouds [*Twomey*, 1974] applies for clouds of constant cloud water, or constant liquid water path (LWP). However, the ability of

0148-0227/02/2001JD001502$09.00

entrained aerosol to affect boundary layer cloudiness through modification of precipitation [e.g., *Albrecht*, 1989], or through absorption heating by the aerosol [*Ackerman et al.*, 2000] suggests that one consider the implications of enhanced aerosol concentrations in a more general framework [e.g., *Han et al.*, 1998; *Brenguier et al.*, 2000]. Thus one might view the aerosol indirect effect as a primary aerosol indirect effect at constant cloud LWP, and secondary indirect effects whereby entrainment of aerosol generates feedbacks that modify LWP. Evidence of modifications to LWP has been observed in ship tracks [e.g., *Coakley and Walsh*, 2000; *Platnick et al.*, 2000], in satellite data [e.g., *Han et al.*, 2002], and in numerical models [e.g., *Ackerman et al.*, 1995].

[4] During the Atlantic Stratocumulus Transition Experiment (ASTEX), two Lagrangian experiments were carried out with extreme variations in aerosol conditions. The first Lagrangian (L1) was characterized by very clean marine air with low aerosol concentration, while the second Lagrangian (L2) took place in a boundary layer with an aged polluted aerosol after a heavily polluted air mass of European origin moved into the study region on 15 June 1992. [e.g., *Huebert et al.*, 1996; *Clarke et al.*, 1996; *Bretherton and Pincus*, 1995; *Bretherton et al.*, 1995]. Most of the research with ASTEX data has focused on either L1 [e.g., *Bretherton et al.*, 1999a; *Duynkerke et al.*, 1995; *De Roode and Duynkerke*, 1997] or L2 [e.g., *Martin et al.*, 1995]. Little attention has been given to the entrainment of aerosol (some subset of which are cloud condensation nuclei (CCN)) from above the inversion into the initially clean marine boundary layer, its impact on cloud microphysical and optical properties, radiative budget, and its potential climatic effects.

[5] In a numerical modeling study of Arctic Stratocumulus Cloud observed on 18 May 1998 during the SHEBA/FIRE Spring IOP, *Jiang et al.* [2001] showed that the entrainment of polluted air of free tropospheric origin into the cloud altered the cloud optical depth and albedo, as well as the boundary layer dynamics by modifying cloud-top cooling rates and drizzle. However, the structure of the Arctic boundary layer is very different from a sub-tropical marine boundary layer. Thus we expect that entrainment rates, and perhaps the mechanism for entrainment, will differ between the Arctic boundary layer and sub-tropical marine boundary layer, with commensurate differences in response.

[6] Numerous studies have addressed the fact that any process that decreases drizzle has the potential to significantly alter the radiative forcing of clouds (e.g., *Albrecht* [1993], *Stevens et al.* [1998], and *Feingold et al.* [1999], among others). The purpose of this paper is to consider the effect of entrainment of long range transported aerosol into the subtropical marine boundary layer under conditions where precipitation is virtually nonexistent. We address several key questions: (1) what is the effect of entrainment of polluted air at cloud top on the marine boundary layer structure and optical properties? (2) how will the boundary layer structure and optical and radiative properties respond to varying levels of subsidence and to the growth rate of cloud-top height? (3) will the fact that entrainment of polluted aerosol and drier, warmer free-tropospheric air occur simultaneously, enhance or diminish the primary aerosol indirect effect?

[7] To address these issues, a number of numerical simulations were performed in a two-dimensional eddy-resolving model (ERM) with liquid-phase, bin-resolving microphysics [*Feingold et al.*, 1996a]. A thermodynamic sounding taken from the island of Santa Maria on 17 June 1992 is used for all the simulations. This day was chosen because it lies between the L1 and L2 when polluted air was being transported to the clean MBL.

[8] The paper is organized as follows: Section 2 contains a brief summary of the ERM and the explicit microphysics model. Section 3 describes the case under scrutiny, and numerical experiment design. Section 4 presents results from two baseline simulations: one using a vertically uniform CCN profile as the control run, and the other using the CCN sounding data collected on 17 June 1992 during ASTEX. The two baseline simulations are repeated with varying levels of subsidence as sensitivity experiments. Sections 5 and 6 discuss and summarize the results.

2. Eddy-Resolving Model

[9] The Regional Atmospheric Modeling System (RAMS) is a multi-purpose modeling system that has been used as a three-dimensional (3-D) large eddy simulation (LES) to simulate drizzle production in marine stratocumulus [*Stevens et al.*, 1998; *Feingold et al.*, 1999] and Arctic stratocumulus [*Jiang et al.*, 2001] and as a two-dimensional (2-D) eddy-resolving model (ERM) to study Arctic boundary layer stratus [*Olsson et al.*, 1998; *Harrington et al.*, 1999; *Jiang et al.*, 2000]. In this investigation RAMS is set up as a non-hydrostatic ERM combined with an explicit microphysics model [*Feingold et al.*, 1994] and a two-stream radiation model [*Harrington et al.*, 2000].

2.1. Explicit Microphysics Model

[10] The explicit bin-resolving microphysics model is the same as the one used by *Jiang et al.* [2001]. Readers are referred to *Tzivion et al.* [1987, 1989] for details. A brief description is given below.

[11] A fixed grid is set up in the range 1.56–504 μm (radius). The range is divided into 25 bins, with mass doubling from one bin to the next. Both the mass and the number mixing ratios are predicted for each bin which requires 50 predictive equations. Only warm microphysical processes are considered: condensation/evaporation, collision-coalescence, droplet activation from CCN, and sedimentation.

[12] We use a simple drop activation scheme [*Stevens et al.*, 1996] in which CCN are assumed to have a constant (in time and space) size distribution and activation is calculated such that the number of cloud drops is based on the model-derived supersaturation but does not exceed the number concentration of CCN. Thus, at each time step the drop concentration N_d is incremented by an amount

$$\Delta N_d = \max\left[0, N_{ccn}\int_{r_{cut}}^{\infty} f(r; r_g, \sigma_g)\,dr - \sum_{k=1}^{25} N_k\right] \qquad (1)$$

where N_{ccn} is the total CCN concentration, r_{cut} is the smallest radius of CCN activated at the ambient supersaturation S, r_g is the median radius of CCN, σ_g is the geometric standard deviation of the CCN radii, and N_k is the number concentration of drops in size bin k. We assume that r_g and σ_g are constant throughout the model domain and that only

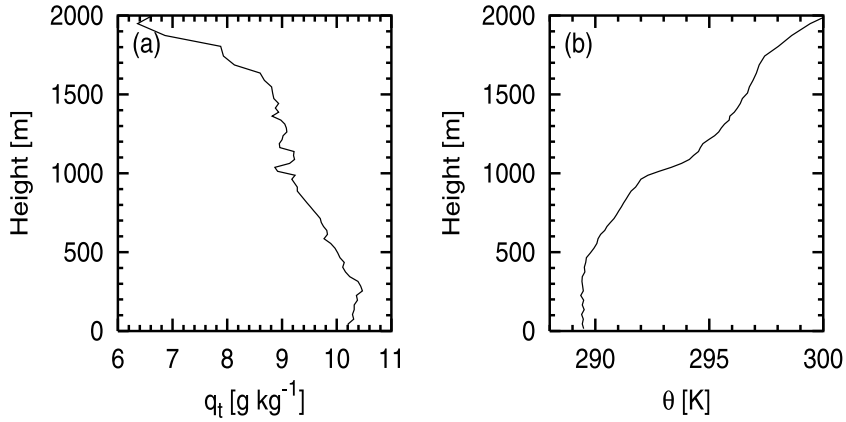

Figure 1. Vertical profiles of the initial conditions: (a) total water mixing ratio and (b) dry potential temperature.

N_{ccn} varies as one passes from the clean boundary layer to the polluted air aloft. The representation of the aerosol is reduced to prognostic N_{ccn}. The simplified treatment assumes that the CCN concentration is unmodified (in both number and size) by the cloud. For clouds with very weak collision-coalescence such as is the case examined here, this is quite reasonable [e.g., *Feingold et al.*, 1996b]. Aqueous chemistry may affect the aerosol size distribution [*Hoppel et al.*, 1990] but this is beyond the scope of this study. For the goals of our study, we feel that this representation is sufficient.

2.2. Boundary Conditions and Numerical Setup

[13] All the simulations are done in a 2-D framework. The domain has 70 × 68 grid points with a 50 m grid spacing in the horizontal and a 30 m grid spacing in the vertical from the surface to the domain top (2220 m). The time step is 2s.

[14] The lateral boundary conditions are cyclic. The boundary condition at the model top corresponds to a rigid lid, with a Rayleigh friction absorbing layer applied to the momentum equations and to the thermodynamic equation. The bottom boundary is specified to be consistent with surface conditions observed during ASTEX, with a specified surface temperature of 293 K.

3. Case Description and Experiment Design

3.1. Case Description

[15] The model is initialized with a sounding taken on the island of Santa Maria at 0719Z on 17 June 1992 during ASTEX. The thermodynamic structure is characterized by a decoupled boundary layer with a weak inversion [*Miller and Albrecht*, 1995].

[16] The initial total water mixing ratio q_t and dry potential temperature θ are given in Figure 1. The initial profiles of θ and q_t consist of three distinct layers: a dry neutral layer below 500 m, a conditionally unstable layer from 500 to 1000 m, and an absolutely stable inversion layer above 1000 m. Note that the moisture content of the inversion layer is relatively high and not significantly different from that in the conditionally unstable air. This is in strong contrast to typical California coastal stratocumulus.

3.2. Experiment Design

[17] As noted in the introduction, the first Lagrangian took place in very clean marine air where CCN concentrations were less than 100 cm^{-3} at a supersaturation of 0.8%. (Henceforth, all concentrations of CCN are quoted with respect to 0.8% supersaturation.) This clean air was replaced by heavily polluted European continental air with CCN values higher than 1200 cm^{-3} during the second Lagrangian [*Albrecht et al.*, 1995]. The case under discussion lies between these two events when polluted air was being transported to the clean MBL.

[18] A number of numerical experiments have been performed to investigate how the entrainment of free tropospheric air, rich in aerosol, into the cloudy boundary layer affects microphysical, optical, and radiative properties of the sub-tropical marine boundary layer. Two baseline simulations are performed. The first has a constant initial CCN profile of 100 cm^{-3}, a value close to that observed on research flight 7 using an Instantaneous CCN Spectrometer [*Hudson*, 1989] during L1 (hereafter referred to as N100-D3, where D3 denotes the mean divergence of 3 × 10^{-6} s^{-1}). In the second baseline simulation, the initial CCN profile retains a value of 100 cm^{-3} in the MBL but jumps to 1200 cm^{-3} at cloud top. This profile is roughly based on CCN data collected during ASTEX research flight 10. This simulation is hereafter referred to as N1200-D3. The initial CCN profile used for the N1200-D3 run, the observed CCN profile, and the constant CCN value used for the N100-D3 are shown in Figure 2. Note that the observed high CCN

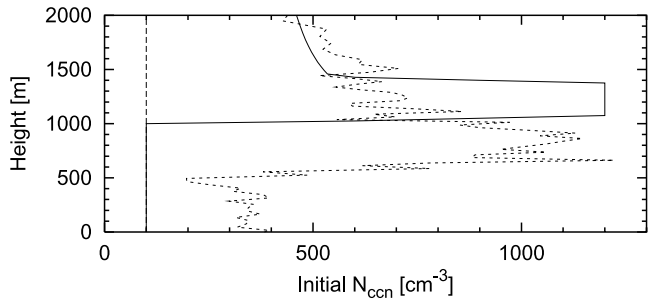

Figure 2. Vertical profile of the initial CCN concentration for the N1200-D3 run (solid line), the CCN profile observed during Research Flight 10 of ASTEX, activated at 0.8% supersaturation (short-dashed line), and the constant initial CCN concentration for the N100-D3 run (long-dashed vertical line).

concentrations extend further into the cloud layer than our idealized profile. We hypothesize that this is because entrainment processes have already contaminated the observed cloud layer. Since the entrainment of aerosol into the cloud layer is the focus of our research, our idealized initial profile contains a clean cloud layer.

[19] In both the N100-D3 and N1200-D3 run and the subsequent sensitivity runs, the large-scale subsidence is prescribed by $w_s = -D \times z$. Where D is the mean horizontal divergence between the surface and the marine inversion, and z is the model height in m. To investigate the sensitivity of the simulated MBL to large-scale subsidence, we repeated the two baseline simulations (N100-D3 and N1200-D3) with various degrees of large-scale subsidence by changing D from zero to $= 6 \times 10^{-6}$ s^{-1}. D is estimated to be 6×10^{-6} s^{-1} for L1 and 3×10^{-6} s^{-1} for L2 [*Bretherton et al.*, 1995]. However, the simulation results with $D > 4 \times 10^{-6}$ s^{-1} suggest that the associated large-scale subsidence is too strong for the marine boundary layer to develop and grow realistically. Therefore we only report on the runs with $D \leq 4 \times 10^{-6}$ s^{-1}. The experiments are summarized in Table 1. The nomenclature of the sensitivity experiments is such that N100-D1 denotes the run with a CCN concentration of 100 cm^{-3} and divergence $D = 1 \times 10^{-6}$ s^{-1}, while N1200-D4 denotes the run with the maximum CCN concentration of 1200 cm^{-3} at the inversion and $D = 4 \times 10^{-6}$ s^{-1}.

Table 1. Description of Experiments[a]

EXP	N_{CCN}, cm^{-3}	D, s^{-1}	w_s at 1400, cm s^{-1}
N100-D0	100	D = 0.0E-6	0.0
N100-D1	100	D = 1.0E-6	−0.14
N100-D2	100	D = 2.0E-6	−0.28
N100-D3	100	D = 3.0E-6	−0.42
N100-D4	100	D = 4.0E-6	−0.56
N1200-D0	1200	D = 0.0E-6	0.0
N1200-D1	1200	D = 1.0E-6	−0.14
N1200-D2	1200	D = 2.0E-6	−0.28
N1200-D3	1200	D = 3.0E-6	−0.42
N1200-D4	1200	D = 4.0E-6	−0.56

[a]See text for details.

4. Simulation Results: Sensitivity Experiments

[20] Selected time-series and mean profiles of different cloud properties averaged over the horizontal (x) plane (referred to as layer averages) and then time-averaged over an hour interval will be shown. First, comparison between the two base runs will be presented and compared with the available observational data. Comparison among the runs with different large-scale subsidences will follow. In general the model requires about 2 h to produce the initial cloud and establish the resolved-scale turbulence. Thus, we will only look at various fields after this spin-up period.

4.1. Sensitivity to CCN Concentration

4.1.1. Thermodynamical Fields

[21] Time-height cross sections of modeled thermodynamical fields are presented in Figure 3 with the N1200-D3 results on the left panel and the N100-D3 results on the right panel. The simulated marine boundary layer is capped by a 2 K inversion (Figures 3a and 3d) throughout the simulation in both runs. A weak inversion can be seen in the total water mixing ratio. Across the inversion, the MBL is only slightly moister (0.2 g kg^{-1}) than the air above the inversion and therefore entrainment of the air from above is not likely to dry the cloud layer significantly. The average value of q_t marking the inversion varies from 9.3 g kg^{-1} at 120 min to 9.0 g kg^{-1} by the end of the simulation. The weak inversion makes it very difficult to compute the entrainment rate based on the horizontally averaged q_t jumps, as will be discussed later.

[22] The layer-averaged liquid water mixing ratio shows a solid stratocumulus layer for the entire simulation for both runs, while a penetrating cumulus cell rises up from the subcloud layer into the stratocumulus at ~300 min in the N100-D3 run (Figure 3f), a feature often observed in the ASTEX cumulus transition regime [e.g., *Miller and Albrecht*, 1995; *Wang and Lenschow*, 1995]. For N1200-D3 the penetrating cumulus convection exists but is much weaker. The liquid water field, q_l, also shows that in both cases the stratocumulus layer thins towards the end of the simulation.

4.1.2. Impact of Weak Drizzle on Boundary Layer Dynamics

[23] The cloud top height, z_t (calculated using a thermodynamic criterion based on the point at which the total mixing ratio q_t just saturates the air at θ_l), and cloud base z_b (similarly defined), grow steadily with time in both the N100-D3 and N1200-D3 run (Figure 4a). The small difference in z_t between the two runs becomes noticeable from 240 min to the end of the simulation with z_t about 20 m higher in the N1200-D3 than in the N100-D3 run. The cloud base height z_b shows considerable fluctuation in both runs, but compares reasonably well with the ceilometer data (Figure 4a, dotted line), collected on the island of Santa Maria (Pennsylvania State University).

[24] In the N100-D3 run, the maximum cloud-base drizzle rate (Figure 4b) of 0.5 mm day^{-1} occurs around 300 min, and about the same time as the cumulus penetration. The time series of column maximum $\sigma_w = (w'w')^{1/2}$ (Figure 4c) shows that maxima in σ_w correspond to the deeper cloud and higher cloud-base drizzle rate, indicating a stronger dynamic response during and immediately after the higher drizzle events at cloud base. It appears that evaporation of drizzle just below cloud base produces a cooler and moister layer which is sufficient to destabilize the subcloud layer (not the entire boundary layer) and promote the development of penetrating cumulus [e.g., *Stevens*, 1996; *Feingold et al.*, 1996a]. The penetrating cumulus supplies more surface water vapor and helps maintain and enhance the LWP (Figure 4d) as shown previously by *Martin et al.* [1995] and *Wang and Lenschow* [1995].

[25] In the N1200-D3 run, however, the cloud-base drizzle rate is only one fifth of that in the N100-D3 run. The increased droplet number in the N1200-D3 run suppresses drizzle formation and cloud base drizzle rates are substantially lower than for N100-D3. Penetrating cumulus are much weaker (Figure 3c) and LWP much lower (Figure 4d). Based on ship track simulation with a 1-D model, *Ackerman et al.* [1995] found that cloud liquid water decreases with decreasing droplet concentrations during daytime. In their calculations, the decrease in cloud liquid water is due to evaporation of droplets below cloud base, thereby reducing the supply of moisture to the cloud layer.

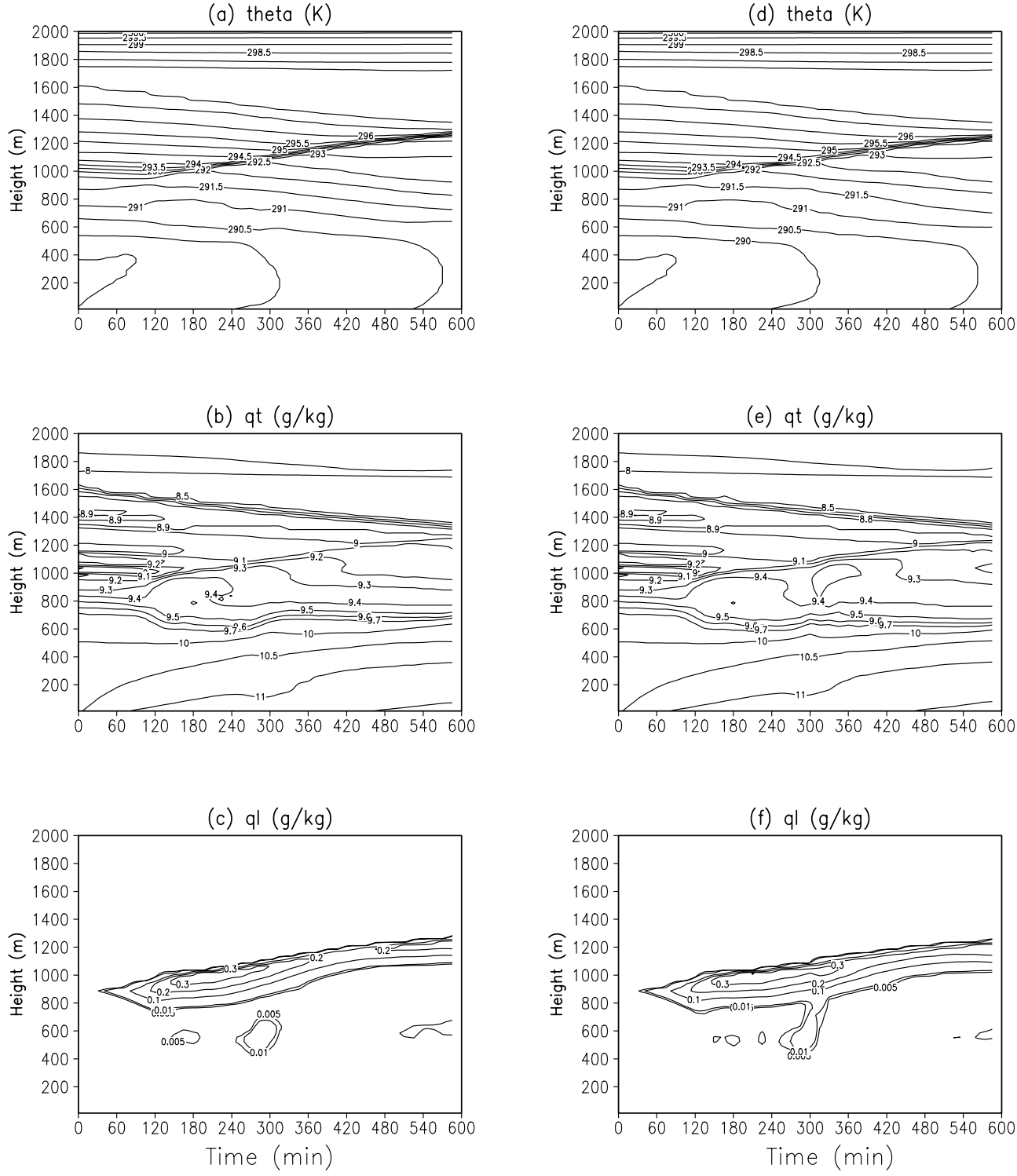

Figure 3. Time-height cross sections of (a, d) θ (contour interval 0.5 K), (b, e) total water mixing ratio q_t (variable contour intervals as labeled), and (c, f) liquid water mixing ratio q_l (the first contour is 0.005 g kg^{-1}, the second contour is 0.01 g kg^{-1}, and the contour interval is 0.1 g kg^{-1} thereafter). The left panels denote the N1200-D3 run and the right panels denote the N100-D3 run.

[26] The role of evaporative cooling just below cloud base in enhancing cumulus convection is investigated further by examining the vertical structure of various variables. Horizontally and temporally averaged profiles over the sixth hour (300 min–360 min) for both the N1200-D3 and N100-D3 run are shown in Figure 5. The profiles examined are: drizzle rate F_{driz}, heating associated with the drizzle (calculated from the divergence of the drizzle flux), lapse rate $d\theta/dz$ (only the region below cloud base is plotted), buoyancy flux $(\overline{w'\theta_v'})$ including contribu-

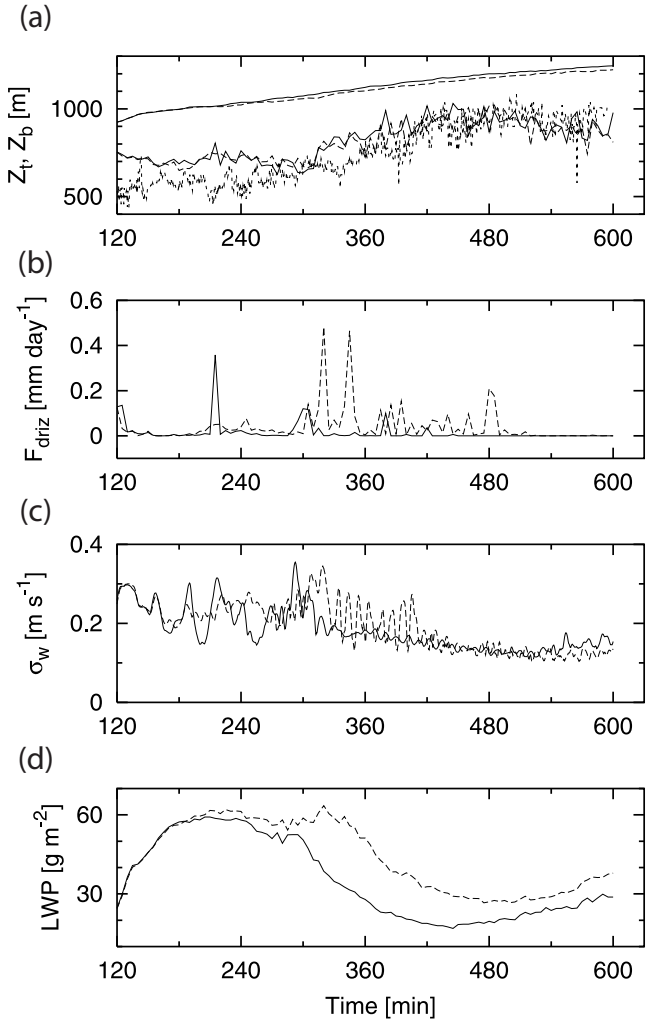

Figure 4. The temporal evolution of (a) cloud top and cloud base, (b) cloud-base drizzle rate, (c) maximum value of $\langle w'w' \rangle^{1/2}$ labeled as σ_w, and (d) LWP. The solid line denotes the N1200-D3 run and the dashed line denotes the N100-D3 run. The dotted line in Figure 4a denotes the ceilometer data collected by Penn State University on the island of Santa Maria.

tions by vapor and heat flux only $\left(\overline{(w'\theta')}[1 + .61\overline{q_v}] + 0.61\bar{\theta}\overline{(w'q_v')}\right)$ [*Stull*, 1988], vertical velocity variance $\overline{(w'w')}$, and cloud fractional area (fraction of grid points that contain cloud water exceeding 0.01 g kg^{-1} over the entire domain). Overbars represent spatial and time averages over the sixth hour of the simulation.

[27] Drizzle (Figure 5a) occurs mainly in the cloud layer with only 3% present below the cloud base in the N100-D3 run, but none reaching the surface for either runs. Evaporation of drizzle will cool and moisten the layer below the cloud base in the N100-D3 run.

[28] The heating associated with the drizzle profiles (Figure 5b) shows that there is a small region below the average level of cloud base where evaporative cooling of drizzle exists and there is about 1 K h^{-1} warming near the cloud top in the N100-D3 run whereas the cooling is approximately zero below cloud base in the N1200-D3 run. This warming will reduce the net radiative cooling at cloud top.

[29] The plot of $d\theta/dz$ (Figure 5c) provides evidence that the cooling from evaporating drizzle induces destabilization with respect to the surface in the layer between 550–700 m. The destabilizing effect only applies to the case when drizzle evaporates completely before reaching the surface [e.g., *Paluch and Lenschow*, 1991; *Feingold et al.*, 1996a]. *Paluch and Lenschow* [1991] differentiated between two scenarios: (1) precipitation reaches the surface and the associated cooling tends to stabilize the entire layer below the cloud; and (2) precipitation evaporates just below cloud and the associated cooling tends to destabilize the layer below cloud. The case under discussion clearly corresponds to the latter. To further strengthen our case that small amounts of drizzle evaporating near cloud base can destabilize the boundary layer, the simulation of N100-D3 was repeated with the initial CCN concentration reduced to 20 cm^{-3}. Drizzle reaches the surface (figure not shown) and does not lead to formation of cumulus under stratus as expected.

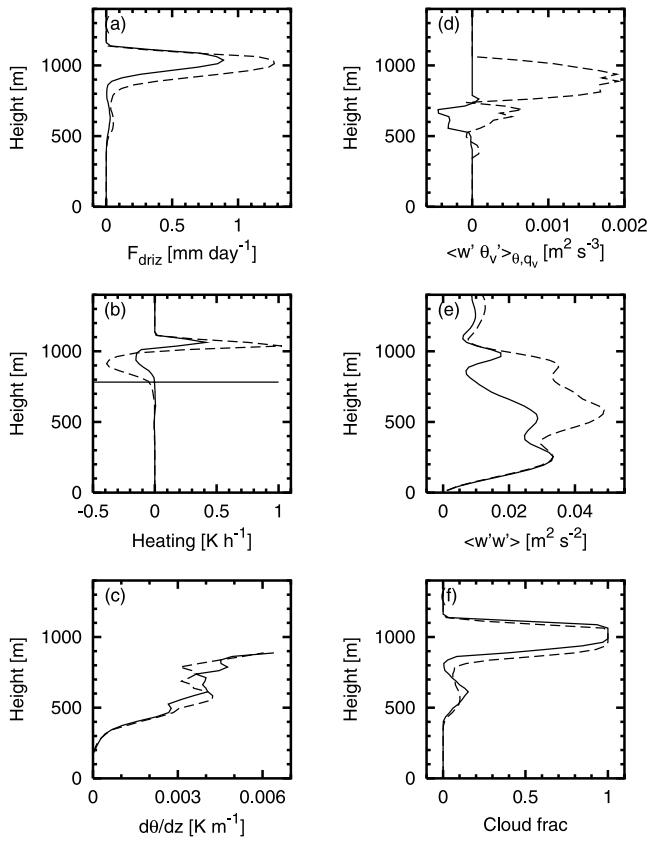

Figure 5. Horizontally averaged profiles of (a) drizzle rate, (b) heating associated with drizzle flux (calculated from the vertical divergence of the drizzle flux), (c) lapse rate $d\theta/dz$, (d) dry buoyancy flux $\langle w'\theta_v' \rangle_{\theta,q_v}$ conditionally sampled over the updraft region with $w \geq 0.4\ m\ s^{-1}$, (e) vertical velocity variance $\langle w'w' \rangle$, and (f) cloud fractional area time averaged over the sixth hour of the simulation for both the N1200-D3 and N100-D3 run. The solid horizontal line in Figure 5b is the average cloud-base height for the N100-D3 run. The solid line denotes the N1200-D3 run and the dashed line denotes the N100-D3 run.

[30] It is noted that the buoyancy flux $(\overline{w'\theta_v'})$ (Figure 5d) is conditionally sampled over the updraft region with $w \geq 0.4$ m s^{-1} to isolate the contribution of the penetrating cumulus. A positive buoyancy flux (Figure 5d) is produced in the layer (500–700 m) where cooling and moistening occurs in association with drizzle evaporation in the N100 run. Detailed analysis of the contributions by heat and vapor flux shows that a positive vapor flux (not shown) is solely responsible for the positive buoyancy flux in the N100-D3 run, while a negative heat flux is the result of cooling in the updraft region in both the N100-D3 and N1200-D3 run.

[31] The positive buoyancy flux is the major source of the stronger vertical motion $(\overline{w'w'})$ (Figure 5e), and promotes penetrating cumulus as reflected in the cloud fractional area. The cloud fractional area shows a solid stratocumulus layer for both runs. The stratocumulus layer is elevated slightly in the N1200-D3 run. The greatest differences, however, occur just below the cloud base. The partial coverage is indicative of the presence of penetrating cumulus below stratocumulus in the N100-D3 run, while the cumulus and stratocumulus are in two separate layers in the N1200-D3 run.

[32] A question is raised whether the surface fluxes might be contributing to the difference in the strength of the penetrating cumulus. Investigation of the magnitude of surface latent heat flux and surface sensible heat flux between the N1200-D3 and N100-D3 cases indicates (figures not shown) that differences in these fluxes are small (order of a few percent) but are slightly larger in the case of N1200-D3. Therefore unlike in the case of precipitating boundary layers with significant surface cooling and moistening, neither surface latent heat flux nor surface sensible heat flux can explain the difference in the strength of the penetrating cumulus.

[33] The above results suggest that even tiny amounts of cloud drizzle can generate subtle feedbacks, and that the entrainment of polluted air will suppress this drizzle and change the structure of the MBL.

4.1.3. Cloud Optical Depth and Albedo

[34] The optical depth (in the visible) is defined as

$$\tau \approx \int_{z_b}^{z_t} \int_0^{\infty} 2\pi r^2 n(r,z) dr dz, \tag{2}$$

where $n(r)$ defines the drop spectrum with respect to radius r and an asymptotic value of 2 has been assumed for the extinction efficiency [e.g., *Platnick and Twomey*, 1994].

[35] The dependence of τ on both LWP and N_d is clearly illustrated in Figure 6a. Higher τ in the N1200-D3 run is associated with higher N_d between 120 and 300 min and between 450 and 600 min even though the LWP is slightly higher for N100-D3. Between 300 and 450 min, however, τ is similar in both cases. For the N1200-D3 run, the entrainment of higher CCN concentration air results in a much higher concentration of droplets, and a smaller drop size. But in spite of this, the significantly lower LWP means that on balance τ is approximately the same as in N100-D3.

[36] Albedo is calculated using the simple relationship between cloud albedo A and optical depth given by *Bohren* [1987].

$$A \approx \frac{(1-g)\tau}{2+(1-g)\tau} \tag{3}$$

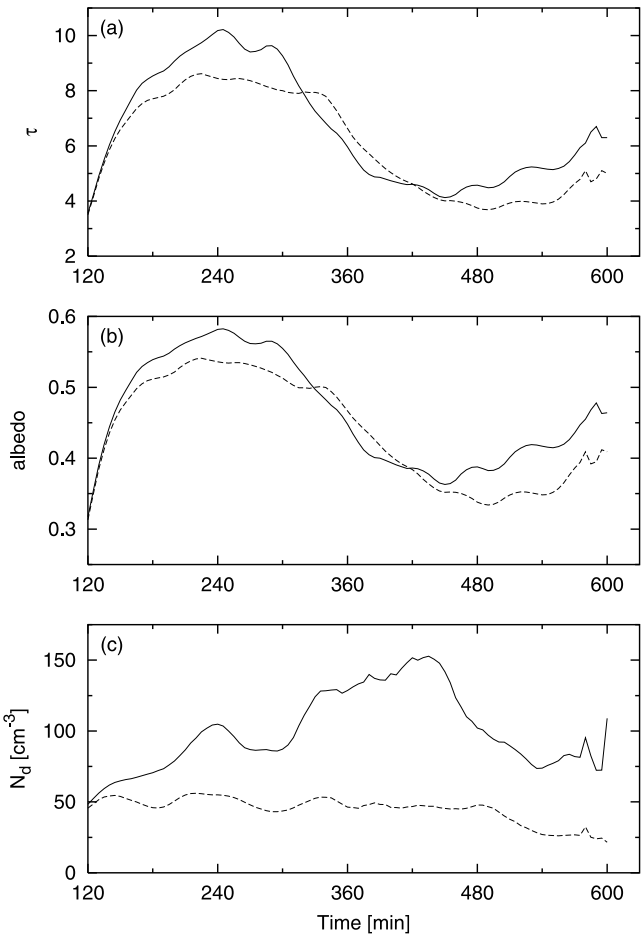

Figure 6. The temporal evolution of (a) cloud optical depth τ, (b) cloud albedo A, and (c) N_d averaged over the cloud depth with line types as indicated in Figure 5.

where g is the scattering asymmetry factor [*Twomey*, 1991]. Since A and τ evolve in a similar manner (Figure 6b), we will only show A in the following sections.

[37] N_d (Figure 6c) fluctuates throughout the simulation, but averages about 100 cm^{-3} for most of the N1200 simulation. Although the boundary layer is progressively contaminated by the dirtier air from above, N_d represents about 10% to 31% of the N_{ccn} in the N1200-D3 run. Note that N_d remains constant at a value of 50 cm^{-3} with N_d decreasing slightly toward the end of the simulation for the N100-D3 run. At any given time, two to four times the number of droplets are competing for the same amount of available water vapor in the N1200-D3 run than in the N100-D3 run. Note that data shown in Figure 6 are smoothed with a 7-point running average to reduce noise.

4.2. Sensitivity to Large-Scale Subsidence

4.2.1. Entrainment Rates

[38] The entrainment rate w_e is normally computed as the average $dz_i/dt - w_s$, where z_i is the local height of the inversion. z_i is not easily determined without knowledge of the total water mixing ratio, buoyancy or ozone eddy fluxes observed at the inversion. As shown in Figure 3b, the modeled q_t at the inversion varies considerably. Instead of finding the local inversion height, an alternative method is

Table 2. Growth Rate of the Cloud-Top Height and LWP Averaged Over the Last Six Hours of Simulation

	N100				N1200			
DIV, s^{-1}	dz_t/dt, cm s^{-1}	$w_s(z_t)$, cm s^{-1}	w_e, cm s^{-1}	LWP, g m^{-2}	dz_t/dt, cm s^{-1}	$w_s(z_t)$, cm s^{-1}	w_e, cm s^{-1}	LWP, g m^{-2}
D0	1.529	0.00	1.529	80.34	1.894	0.00	1.894	69.37
D1	1.318	−0.127	1.445	66.93	1.792	−0.133	1.925	45.65
D2	0.993	−0.240	1.233	48.41	1.340	−0.251	1.591	39.11
D3	0.930	−0.341	1.271	41.64	0.962	−0.346	1.308	30.36

used here. Following *Moeng et al.* [1999], the local cloud-top height $z_{top}(x)$ of a column is calculated (Figure 4a) and $z_{top}(x)$ is then horizontally averaged to find the mean cloud-top height z_t, and hence dz_t/dt. When the large-scale subsidence is nonzero in the simulation, the entrainment rate is defined as $w_e = dz_t/dt - w_s$. The growth rate of the cloud-top height, the w_s value at z_t, and LWP averaged over the last six hours of simulation for selected runs are shown in Table 2. Note that $|w_s(z_t)|$ increases downward in columns 3 and 7 as D values increase. Comparison between the two base simulations (N100-D3 and N1200-D3) shows that the cloud top grows slightly faster in the N1200-D3 run than it does in the N100-D3 run. In general, the N1200 series runs entrain more and the cloud top grows faster than those in the N100 series. Drizzle at cloud base may not remove water from cloud effectively, but the warming (calculated from drizzle flux, Figure 5b) at the cloud top reduces the net cooling (sum of radiative cooling and warming due to drizzle) resulting in less entrainment in the N100 runs.

[39] As $|w_s|$ increases, the entrainment rate decreases, and so does the LWP. Note that LWP is higher in the N100 run than that in the N1200 run for all $|w_s|$ values, suggesting that the drizzle feedbacks to enhanced CCN mechanism we proposed in this study holds for all subsidence rates.

[40] The modeled w_e ranging from 1.89 cm s^{-1} to 1.31 cm s^{-1} is somewhat greater than estimates from the observational data 0.9 (±0.5) cm s^{-1} to 1.2 (±1.0) cm s^{-1} for L1 [*De Roode and Duynkerke*, 1997; *Duynkerke et al.*, 1995; *Bretherton et al.*, 1995] and 0.6 (±0.3) cm s^{-1} for L2 [*Bretherton et al.*, 1995]. However, a factor of 2 uncertainty in observations is the norm since these are derived from large-scale analyses. In addition, *Bretherton et al.* [1999b] showed that 2-D models have a bias toward higher entrainment rates than 3-D models.

[41] The entrainment rate is about twice to three times higher in MBL than that in the arctic boundary layer (ABL) [*Jiang et al.*, 2001]. The cloud top radiative cooling is largely responsible for the higher entrainment in the polluted case in both the MBL and ABL except that the case in the current study is more complex because of the existence of penetrating cumulus below stratocumulus.

4.2.2. LWP, Cloud Albedo, and n_d

[42] Time series of LWP, cloud albedo, and N_d averaged over the depth of the cloud layer from the N1200 runs with various levels of large-scale subsidence are shown in Figure 7. Note that data shown in Figure 7 are smoothed with a 7-point running average to reduce noise. Not only is the cloud top height affected [*Schubert et al.*, 1979], but many of the effects of varying w_s are well illustrated in Figure 7. As $|w_s|$ decreases, the cloud liquid water path increases (Figure 7a) [*Chen and Cotton*, 1987] in association with deeper cloud, becomes more reflective (Figure 7b), as more and more CCN entrained and activated to form droplets (Figure 7c). Note that N_d does not response to the changes in $|w_s|$ linearly as LWP and albedo do. It is likely due to the averaging over the cloud depth. It should be noted that for the N100 simulations LWP (not shown) responds to the changes in w_s in a qualitatively similar manner to the N1200 runs except that LWP is higher in the N100 runs (Table 2).

[43] The differences in cloud structure and optical properties in response to the various w_s have a considerable impact on the radiative fluxes. As the cloud becomes more reflective with decreasing $|w_s|$ (Figure 7b), less solar radiation reaches the surface (Figure 8). Comparison between the N1200-D0 and N1200-D3 run reveals that there is a 34% reduction in the downwelling radiative fluxes at the surface in the N1200-D0 run compared to the N1200-D3 run (Figure, 8 solid lines). For the same w_s value higher solar fluxes reach the surface (dashed lines) in the N100 runs than in the N1200 series runs. The biggest difference in F_{sfc}^{-} is 28%, which occurs when w_s is zero.

4.2.3. Changes in Albedo

[44] As discussed in Figure 6, changes in albedo can be a result of either entrainment of high concentrations of CCN

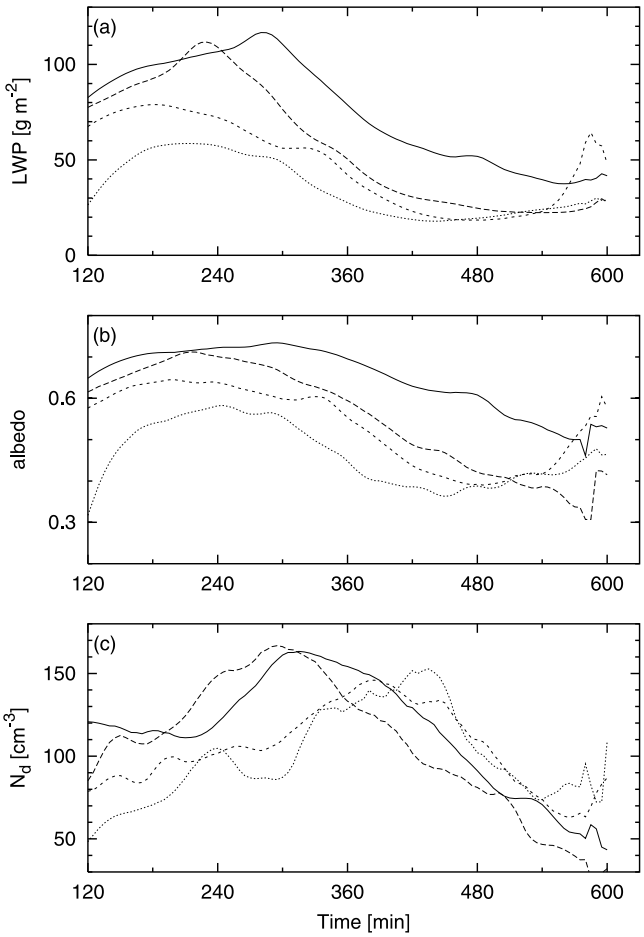

Figure 7. The temporal evolution of (a) LWP, (b) cloud albedo, and (c) droplet number averaged over the depth of the cloud layer. Line types are as follows: for N1200-D0, solid; for N1200-D1, long-dashed; for N1200-D2, short-dashed; and for N1200-D3, dotted.

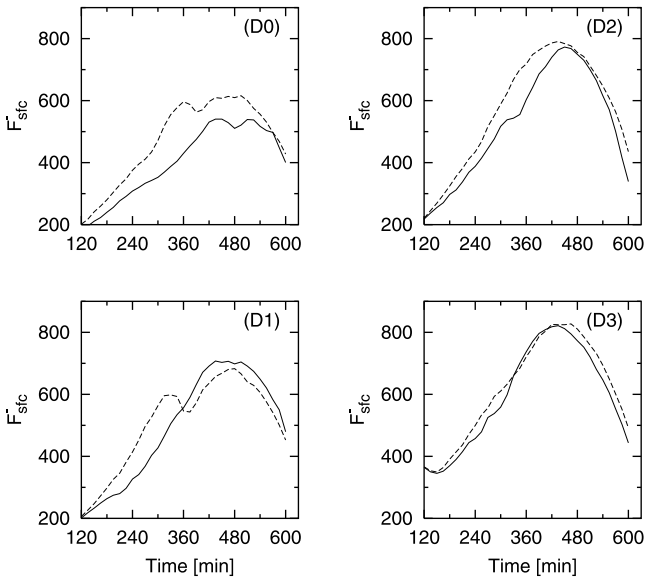

Figure 8. The temporal evolution of downwelling shortwave fluxes at the surface for all the runs with the corresponding divergence value labeled on the upper right corner of each panel (see Table 1). The solid lines denote the N1200 runs and the dashed lines denote the N100 runs.

which affects the number and size of CCN, or changes in LWP. To distinguish the contribution from microphysical and dynamical responses, the albedo averaged over the sixth hour is plotted as a function of subsidence rate (Figure 9a). Also plotted in Figure 9a is the albedo for clouds of similar LWP as a function of subsidence rate (dotted lines) for the N1200 series runs. These points were obtained by comparing clouds of similar LWP (within 1%) regardless of time.

[45] Several features are noteworthy in Figure 9a. The dotted line shows that albedo increases with decreasing subsidence rate for clouds of similar LWP. The change in albedo results from the microphysical response; greater entrainment of higher CCN air results in higher concentrations of droplets, and consequently more reflective clouds [e.g., *Twomey*, 1974]. The solid line shows that albedo increases more rapidly with decreasing subsidence because the LWP increases with decreasing subsidence (Figure 7a). Thus for this case dynamical feedbacks related to entrainment result in an enhancement in the albedo response.

[46] A similar plot to Figure 9a is presented for a series of simulations where the CCN concentration was assumed to be a constant value of 1200 cm^{-3} through the depth of the model domain (Figure 9b). It should be noted that these runs are not listed in Table 1, and are only used to further illustrate the microphysical feedbacks. Comparing with Figure 9a, the results for clouds of similar LWP (dotted line) are, as expected, constant. The slope of the solid line (indicating the response regardless of LWP) is comparable to that in Figure 9a, suggesting similar dynamical response and similar increases in LWP as a function of w_s.

5. Discussion

[47] Two primary sets of results have been shown. The first consists of a comparison between two baseline simulations that differ only in their vertical profiles of aerosol concentration: one has an elevated pollution layer at or above cloud top while the second is relatively clean and the aerosol concentration is constant with height (Figure 2). The second set of results explores the effect of changing levels of large-scale subsidence on these baseline simulations, primarily to explore the extent to which varying subsidence rates affect entrainment of aerosol into the cloud, and feedbacks to cloud optical properties.

5.1. Effect of a Polluted Layer: Constant Subsidence

[48] Figures 3, 4, and 5 show that an elevated polluted layer residing in the free tropospheric air can have a large effect on both cloud microphysics, as well as cloud dynamics. The role of penetrating cumulus in supplying stratocumulus cloud moisture in the warm ocean regime is well known and these results have exemplified the extent to which this process is sensitive to variations in aerosol concentration. Although neither of the baseline simulations can be characterized as drizzling cases (no drizzle reaches the surface in either case, and even the cloud base drizzle rates are only on the order of 1 mm day^{-1}), small amounts of drizzle evaporating beneath cloud base in the clean case (N100-D3) strengthen cumulus transport relative to the case with the elevated pollution layer (N1200-D3). The result is a significantly enhanced LWP for N100-D3 (Figure 4d). In terms of the effect of the elevated pollution layer on cloud albedo, two effects tend to counter one another. The first is an enhancement in albedo as a result of entrainment of air rich in CCN into the cloud [see also *Duda et al.*, 1996]. The second is a suppression of LWP due to weaker penetrating cumulus. On balance, the cloud albedo is hardly changed for a significant portion of the simulation (300 min–460

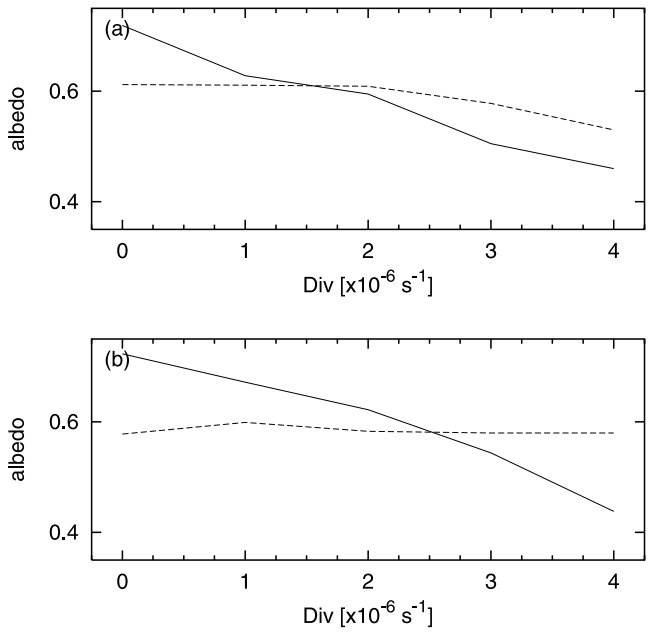

Figure 9. Cloud albedo as a function of divergence (w_s). The solid lines denote cloud albedo time averaged over the sixth hour, while the short-dashed lines denote cloud albedo for clouds with similar LWP, but at different simulation times. (a) the N1200 runs and (b) a new set of constant CCN runs with N_{ccn} = 1200 cm^{-3}.

min, Figure 6). Between 100 and 300 min and between 460 and 600 min the enhanced droplet concentrations in N1200-D3 tip the scales in the direction of higher albedo, albeit at a level reduced from what would be expected from the primary "Twomey Effect" where albedo enhancement is considered at constant LWP. The dynamical feedback has therefore acted to minimize the classical aerosol indirect effect.

[49] The higher LWP in the clean N100-D3 case may be somewhat unique to the current case study. In a shallow boundary layer overlying a cool ocean surface, penetrating cumulus are not active except in heavily drizzling situations [*Stevens et al.* 1998]. Under conditions of weak drizzle our prior simulations of shallow boundary layer clouds [*Olsson et al.*, 1998; *Harrington et al.*, 2000; *Jiang et al.*, 2001] indicated that polluted air affected cloud microphysics and dynamics primarily by suppressing drizzle, as well as through subtle changes in cloud top radiative cooling responding to droplet size. In those simulations, higher aerosol concentrations tended to increase LWP, rather than decrease it in this study.

[50] According to *Stevens et al.* [1998] weakly drizzling clouds may be able to sustain higher LWP longer than non-drizzling clouds by suppressing cloud top entrainment of dry inversion air. This is consistent with the trend in our simulations. However, the similarities may be misleading because that study considered a much shallower L1 MBL ($\approx$800m). Ultimately, the LWP is determined by the net effect among surface moisture fluxes, cloud top radiative cooling, entrainment, and drizzle fluxes. The net results among these will be case dependent so that generalizations should be avoided.

5.2. Effect of a Polluted Layer: Varying Subsidence

[51] The large-scale subsidence velocity controls the rate of rise of the cloud top height, and in this study, the magnitude of entrainment of polluted air. Our results show that the cloud structure of the modeled marine boundary layer is quite sensitive to the specified large-scale subsidence as shown previously by *Chen and Cotton* [1987]. In the current study, the rather moist inversion layer (Figure 1) limits entrainment drying, and in fact as subsidence is decreased, the LWP increases (Figure 7). The combined effects of increased LWP as well as higher drop concentrations cause significant enhancements in albedo. Cloud albedo increases by about 36% as cloud top subsidence varies from -0.4×10^{-2} m s^{-1} to zero for the N1200 series runs. The changes in albedo directly affects the incident solar flux at the surface. Incident solar flux reaching the surface is reduced by 38% when cloud albedo is highest.

[52] As shown in Figure 9, one can separate the effects of the albedo increase due to the increase in aerosol concentration, from those due to increased LWP. When comparing clouds with equal LWP, as in the classical evaluation of the primary indirect effect, the N1200 simulations indicate an albedo that increases slowly with decreasing subsidence. When one relaxes the constraint of constant LWP the albedo increase is significantly enhanced. Thus, contrary to the baseline simulation results for constant subsidence, here the two factors influencing albedo work in unison to create a positive feedback. It should be noted that the enhanced albedo should largely be attributed to large-scale dynamics since the decreased large-scale subsidence is responsible for the increased LWP (Figure 7a).

6. Summary

[53] Results from two baseline, eddy-resolving simulations of the 17 June 1992 ASTEX case have been presented. One simulation uses the thermodynamic and CCN sounding data taken from the ASTEX research flight RF10 (17 June 1992). The other uses a CCN profile of smaller constant value taken from research flight RF07. Twelve sensitivity experiments repeating the two baseline simulations with varying levels of large-scale subsidence are performed.

[54] The major results of this study may be summarized as follows. The two baseline simulations study the response of the modeled marine boundary layer to the change in CCN concentration. As the polluted air (higher N_{ccn}) is entrained into the cloudy boundary layer, droplet number N_d increases and effective radii decreases. However, due to a subtle feedback to boundary layer dynamics, penetrating cumulus convection is weakened and LWP is significantly reduced. The result is that on balance, cloud albedo is not significantly affected by the entrained polluted air. The classical primary aerosol indirect effect whereby enhanced aerosol concentrations result in higher droplet concentrations and more reflective clouds is therefore minimized.

[55] The mechanism responsible for stronger penetrating cumulus in the lower N_{ccn} case is identified. It is shown that the presence of small amounts of drizzle evaporating just below cloud base destabilizes this region with respect to the surface. This should be contrasted with situations where drizzle falls to the surface and the associated cooling stabilizes the entire boundary layer [*Paluch and Lenschow*, 1991; *Feingold et al.*, 1996a].

[56] The series of simulations of the sensitivity of the modeled marine boundary layer to varying degrees of large-scale subsidence indicate that large-scale subsidence not only affects cloud top height [*Schubert et al.*, 1979; *Chen and Cotton*, 1987], and boundary layer structure [*Turton and Nicholls*, 1987], but also has a significant impact on cloud microphysical and optical properties, entrainment rate, and consequently the radiative budget. For the current case study, enhanced cloud top entrainment of polluted air and the increased LWP in response to a decrease in large-scale subsidence result in an enhanced albedo that is much stronger than that due purely to the primary aerosol indirect effect as defined by *Twomey* [1974, 1977].

[57] The results presented here have demonstrated that dynamical feedbacks associated with entrainment of polluted air into the MBL may either reduce or enhance the aerosol indirect effect, depending on the large-scale synoptic conditions and aerosol air mass properties. Although the results are case specific, they do indicate that, in general, quantification of the aerosol indirect effect presents a formidable challenge.

[58] **Acknowledgments.** The comments of Qingyuan Han and an anonymous reviewer greatly improved the clarity of this manuscript. This research was supported by grants from the NSF under grant ATM-9904128. G. Feingold was supported by the NOAA/NSF EPIC program. The observational data used in this study were obtained from the NASA Langley Research Center Atmospheric Sciences Data Center.

References

Ackerman, A. S., O. B. Toon, and P. V. Hobbs, Numerical modeling of ship tracks produced by injections of cloud condensation nuclei into marine stratiform clouds, *J. Geophys. Res.*, *100*, 7121–7133, 1995.

Ackerman, A. S., O. B. Toon, J. P. Taylor, D. W. Johnson, P. V. Hobbs, and R. J. Ferek, Effects of aerosols on cloud albedo: Evaluation of Twomey's parameterization of cloud susceptibility using measurements of ship tracks, *J. Atmos. Sci.*, *57*, 2684–2695, 2000.

Albrecht, B. A., Aerosols, cloud microphysics, and fractional cloudiness, *Science*, *245*, 1227–1230, 1989.

Albrecht, B. A., Effects of precipitation on the thermodynamic structure of the trade wind boundary layer, *J. Geophys. Res.*, *98*, 7327–7337, 1993.

Albrecht, B. A., C. S. Bretherton, D. Johnson, W. H. Scubert, and A. S. Frisch, The Atlantic Stratocumulus Transition Experiment: ASTEX, *Bull. Am. Meteorol. Soc.*, *76*, 889–904, 1995.

Bohren, C. F., Multiple scattering of light and some of its observable consequences, *Am. J. Phys.*, *55*, 524–533, 1987.

Brenguier, J.-L., H. Pawlowska, L. Schuller, R. Preusker, J. Fischer, and Y. Fouquart, Radiative properties of boundary layer clouds: Droplet effective radius versus number concentration, *J. Atmos. Sci.*, *57*, 803–821, 2000.

Bretherton, C. S., and R. Pincus, Cloudiness and marine boundary layer dynamics in the ASTEX lagrangian experiments, part I, Synoptic setting and vertical structure, *J. Atmos. Sci.*, *52*, 2707–2723, 1995.

Bretherton, C. S., P. Austin, and S. T. Siems, Cloudiness and marine boundary layer dynamics in the ASTEX lagrangian experiments, part II, Cloudiness, drizzle, surface fluxes, and entrainment, *J. Atmos. Sci.*, *52*, 2724–2735, 1995.

Bretherton, C. S., S. K. Krueger, M. C. Wyant, P. Bethtold, E. Van Meijgaard, B. Stevens, and J. Teixeira, A GCSS boundary-layer cloud model intercomparison study of the first ASTEX Lagrangian experiment, *Boundary Layer Meteorol.*, *93*, 341–380, 1999a.

Bretherton, C. S., et al., An intercomparison of radiatively driven entrainment and turbulence in a smoke cloud, as simulated by different numerical models, *Q. J. R. Meteorol. Soc.*, *125*, 391–423, 1999b.

Chen, C., and W. R. Cotton, The physics of the marine stratocumulus-capped mixed layer, *J. Atmos. Sci.*, *44*, 2951–2977, 1987.

Clarke, A. D., T. Uehara, and J. N. Porter, Lagrangian evolution of an aerosol column during the Atlantic Stratocumulus Transition Experiment, *J. Geophys. Res.*, *101*, 4351–4362, 1996.

Coakley, A. J., Jr., and C. D. Walsh, Limits to the aerosol indirect radiative effect derived from observations of ship tracks, *J. Atmos. Sci.*, *59*, 668–680, 2000.

Curry, J. A., et al., FIRE Arctic clouds experiment, *Bull. Am. Meteorol. Soc.*, *81*, 5–29, 2000.

De Roode, S. R., and P. G. Duynkerke, Observed Lagrangian transition of stratocumulus into cumulus during ASTEX: Mean state and turbulence structure, *J. Atmos. Sci.*, *54*, 2157–2173, 1997.

Duda, D. P., G. L. Stephens, B. Stevens, and W. R. Cotton, Effects of aerosol and horizontal inhomogeneity on the broadband albedo of marine stratus: Numerical simulations, *J. Atmos. Sci.*, *53*, 3757–3769, 1996.

Duynkerke, P. G., H. Q. Zhang, and P. J. Jonker, Microphysical and turbulent structure of nocturnal stratocumulus as observed during ASTEX, *J. Atmos. Sci.*, *52*, 2778–2787, 1995.

Feingold, G., B. Stevens, W. R. Cotton, and R. L. Walko, An explicit cloud microphysical/LES model designed to simulate the Twomey effect, *Atmos. Res.*, *33*, 207–233, 1994.

Feingold, G., B. Stevens, W. R. Cotton, and A. S. Frisch, The relationship between drop in-cloud residence time and drizzle production in numerically simulated stratocumulus clouds, *J. Atmos. Sci.*, *53*, 1108–1122, 1996a.

Feingold, G., S. M. Kreidenweis, B. Stevens, and W. R. Cotton, Numerical simulation of stratocumulus processing of cloud condensation nuclei through collision-coalescence, *J. Geophys. Res.*, *101*, 21,391–21,402, 1996b.

Feingold, G., W. R. Cotton, S. M. Kreidenweis, and J. T. Davis, Impact of giant cloud condensation nuclei on drizzle formation in marine stratocumulus: Implications for cloud radiative properties, *J. Atmos. Sci.*, *56*, 4100–4117, 1999.

Han, Q., W. B. Rossow, J. Chou, and R. M. Welch, Global survey of the relationships of cloud albedo and liquid water path with droplet size using ISCCP, *J. Clim.*, *11*, 1516–1528, 1998.

Han, Q., W. B. Rossow, J. Zeng, and R. M. Welch, Three different behaviors of liquid water path of water clouds in aerosol-cloud interactions, *J. Atmos. Sci.*, *59*, 726–735, 2002.

Harrington, J. Y., T. Reisin, W. R. Cotton, and S. M. Kreidenweis, Cloud resolving simulations of Arctic stratus, part II, Transition-season clouds, *Atmos. Res.*, *51*, 45–75, 1999.

Harrington, J. Y., G. Feingold, and W. R. Cotton, Radiative impacts on the growth of a population of drops within simulated summertime arctic stratus, *J. Atmos. Sci.*, *57*, 766–785, 2000.

Hoppel, W. A., J. W. Fitzgerald, G. M. Frick, and R. E. Larson, Aerosol size distributions and optical properties found in the marine boundary layer over the Atlantic ocean, *J. Geophys. Res.*, *95*, 3659–3686, 1990.

Hudson, J. G., An instantaneous CCN spectrometer, *J. Atmos. Oceanic Technol.*, *6*, 1055–1065, 1989.

Huebert, B. J., A. Pszenny, and B. Blomquist, The ASTEX/MAGE experiment, *J. Geophys. Res.*, *101*, 4319–4329, 1996.

Jiang, H., W. R. Cotton, J. O. Pinto, J. A. Curry, and M. J. Weissbluth, Cloud resolving simulations of mixed-phase Arctic stratus observed during BASE: Sensitivity to concentration of ice crystals and large-scale heat and moisture advection, *J. Atmos. Sci.*, *57*, 2105–2117, 2000.

Jiang, H., G. Feingold, W. R. Cotton, and P. G. Duynkerke, Large-eddy simulations of entrainment of cloud condensation nuclei into the Arctic boundary layer: 18 May 1998 FIRE/SHEBA case study, *J. Geophys. Res.*, *106*, 15,113–15,122, 2001.

Martin, G. M., D. W. Johnson, D. P. Rogers, P. R. Jonas, P. Minnis, and D. A. Hegg, Observations of the interaction between cumulus clouds and warm stratocumulus clouds in the marine boundary layer during ASTEX, *J. Atmos. Sci.*, *52*, 2902–2922, 1995.

Miller, M. A., and B. A. Albrecht, Surface-based observations of mesoscale cumulus-stratocumulus interaction during ASTEX, *J. Atmos. Sci.*, *52*, 2809–2826, 1995.

Moeng, C.-H., P. P. Sullivan, and B. Stevens, Including radiative effects in an entrainment rate formula for buoyancy-driven PBLs, *J. Atmos. Sci.*, *56*, 1031–1049, 1999.

Olsson, P. Q., J. Y. Harrington, G. Feingold, W. R. Cotton, and S. M. Kreidenweis, Exploratory cloud-resolving simulations of boundary-layer Arctic stratus clouds, part I, Warm-season clouds, *Atmos. Res.*, *47–48*, 573–597, 1998.

Paluch, I. R., and D. H. Lenschow, Stratiform cloud formation in the marine boundary layer, *J. Atmos. Sci.*, *48*, 2141–2158, 1991.

Platnick, S., and S. Twomey, Determining the susceptibility of cloud albedo to changes in droplet concentration with the advance very high resolution radiometer, *J. Appl. Meteorol.*, *33*, 334–347, 1994.

Platnick, S., P. A. Durkee, K. Nielsen, J. P. Taylor, S.-C. Tsay, M. D. King, R. J. Ferek, P. V. Hobbs, and J. W. Rottman, The role of background cloud microphysics in the radiative formation of ship tracks, *J. Atmos. Sci.*, *57*, 2607–2624, 2000.

Schubert, W. H., J. S. Wakefield, E. J. Steiner, and S. K. Cox, Marine stratocumulus convection, part II, Horizontally inhomogeneous solutions, *J. Atmos. Sci.*, *36*, 1308–1324, 1979.

Stevens, B., On the dynamics of precipitating stratocumulus, thesis, 140 pp., Colo. State Univ., Fort Collins, Oct. 1996.

Stevens, B., G. Feingold, W. R. Cotton, and R. L. Walko, Elements of the microphysical structure of numerically simulated nonprecipitating stratocumulus, *J. Atmos. Sci.*, *53*, 980–1006, 1996.

Stevens, B., W. R. Cotton, G. Feingold, and C.-H. Moeng, Large-eddy simulations of strongly precipitating, shallow, stratocumulus-topped boundary layers, *J. Atmos. Sci.*, *55*, 3616–3638, 1998.

Stull, R. B., *An Introduction to Boundary Layer Meteorology*, Kluwer Acad., Norwell, Mass., 1988.

Turton, J. D., and S. Nicholls, A study of the diurnal variation of stratocumulus using a multiple mixed layer model, *Q. J. R. Meteorol. Soc.*, *113*, 969–1009, 1987.

Twomey, S., Pollution and planetary albedo, *Atmos. Environ.*, *8*, 1251–1265, 1974.

Twomey, S., The influence of pollution on the short wave albedo of clouds, *J. Atmos. Sci.*, *34*, 1149–1152, 1977.

Twomey, S., Aerosols, clouds and radiation, *Atmos. Environ., Part A*, *25*, 2435–2442, 1991.

Tzivion, S., G. Feingold, and Z. Levin, An efficient numerical solution to the stochastic collection equation, *J. Atmos. Sci.*, *44*, 3139–3149, 1987.

Tzivion, S., G. Feingold, and Z. Levin, The evolution of raindrop spectra, part II, Collisional collection/breakup and evaporation in a rain shaft, *J. Atmos. Sci.*, *46*, 3312–3327, 1989.

Wang, Q., and D. H. Lenschow, An observational study of the role of penetrating cumulus in a marine stratocumulus-topped boundary layer, *J. Atmos. Sci*, *52*, 2778–2787, 1995.

W. R. Cotton and H. Jiang, Department of Atmospheric Science, Colorado State University, Fort Collins, CO 80523, USA. (cotton@atmos.colostate.edu; jiang@atmos.colostate.edu)

G. Feingold, Environmental Technology Laboratory, NOAA, 325 Broadway, Boulder, CO 80305, USA. (graham.feingold@noaa.gov)